Nat Hazards
DOI 10.1007/s11069-017-2753-2

ORIGINAL PAPER

Hybrid broadband simulation of strong-motion records from the September 16, 1978, Tabas, Iran, earthquake (M_w 7.4)

H. Vahidifard[1] · H. Zafarani[2] · S. R. Sabbagh-Yazdi[1]

Received: 4 July 2016 / Accepted: 9 January 2017

Abstract This paper presents a simulation of three components of near-field ground shaking recorded during the main shock at three stations of the September 16, 1978, Tabas ($M_w = 7.4$), Iran, earthquake, close to the causative fault. A hybrid method composed of a discrete wavenumber method developed by Bouchon (Bouchon in Bull Seismol Soc Am 71:959–971, 1981; Cotton and Coutant in Geophys J Int 128:676–688, 1997) and a stochastic finite-fault modeling based on a dynamic corner frequency proposed by Motazedian and Atkinson (Bull Seismol Soc Am 95:995–1010, 2005), modified by Assatourians and Atkinson (Bull Seismol Soc Am 97:935–1949, 2007), is used for generating the seismograms at low (0.1–1.0 Hz) and high frequencies (1.0–20.0 Hz), respectively. The results are validated by comparing the simulated peak acceleration, peak velocity, peak displacement, Arias intensity, the integral of velocity squared, Fourier spectrum and acceleration response spectrum on a frequency-by-frequency basis, the shape of the normalized integrals of acceleration and velocity squared, and the cross-correlation with the observed time-series data. Each characteristic is compared on a scale from 0 to 10, with 10 being perfect agreement. Also, the results are validated by comparing the simulated ground motions with the modified Mercalli intensity observations reported by reconnaissance teams and showed reasonable agreement. The results of the present study imply that the damage distribution pattern of the 1978 Tabas earthquake can be explained by the source directivity effect.

✉ H. Vahidifard
hesam_vf@yahoo.com; hvahidifard@mail.kntu.ac.ir

H. Zafarani
h.zafarani@iiees.ac.ir; hamzafarani@yahoo.com

[1] K. N. Toosi University of Technology, 470 Mirdamad Ave. West, P.O. Box: 15875-4416, 1969764499 Tehran, Iran

[2] International Institute of Earthquake Engineering and Seismology (IIEES), Tehran, Iran

Published online: 30 January 2017

Keywords Hybrid broadband simulation · Near field · Tabas earthquake · MMI observation · Discrete wavenumber method · Stochastic modeling technique

1 Introduction

The Iranian plateau is composed of various seismotectonic regions that can be separated according to their specific characteristics. Tabas is located in the Khorasan part of the Central Iranian seismotectonic province. This zone is bounded to the southwest and northeast by the two "Marginal Active Folded Belts" of "Zagros" and "Koppeh Dagh." Unlike the two areas, central Iran is not a linear seismic zone. It is characterized by scattered seismic activity with large magnitudes and long recurrence periods, together with seismic gaps, along several recent Quaternary faults. The shocks in central Iran are generally shallow and usually involve associated surface breakage (Berberian 1976; Berberian et al. 1979).

A comprehensive seismic hazard and seismicity assessment for Tabas is difficult due to lack of historical data (data recorded before the nineteenth century) in this region. In fact, no evidence accounts for observing seismic damage in or around Tabas over the past 11 centuries (Berberian 1979a). Lack of destructive earthquakes or observing no significant seismic damage in Tabas or its vicinity since the seventh century can be attributed to three factors including poor communication with the rest of the country, lack of sufficient historical seismic data or the essence of earthquakes in Iran's central seismic zone that are generally large magnitude events with long return periods (Berberian 1976).

As another indication of observing no seismic damage in Tabas, Berberian (1979a) refers to historical monuments that were built in this city in the eleventh century which have remained undamaged until the devastating earthquake of 1978. Approximately a year prior to this catastrophic event, the earthquake of September 26, 1977, struck the city of Tabas. Berberian (1979a) believes that in addition to two other earthquakes, this earthquake may represent the long-term seismic precursor of the catastrophic event of 1978. Figure 1 illustrates some information about the three seismic events that occurred prior to the Tabas major earthquake. These events caused seismic damages to local areas close to Tabas city (Berberian 1976).

The earthquake of September 16, 1978, occurred at 15:35:56 UT, in the Khorasan province of east-central Iran with an estimated moment magnitude of about 7.4. The earthquake occurred due to a unilaterally propagating complex rupture process on a thrust fault system. Using a kinematically consistent deformation model, which weight geologic and geodetic data in a rigorous manner to estimate fault slip rates, Khodaverdian et al. (2015) have proposed a low slip rate of $\sim$1.1 mm for the Tabas fault. At the obtained value, the empirical relationships linking the average displacements with earthquake magnitude (Wells and Coppersmith 1994) results that the recurrence time of large earthquakes is around more than 2000 years (no aseismic deformation). The imprints of rupture of four (and possibly five) asperities (sub-faults) have been identified on the recorded accelerograms (Sarkar et al. 2005). This earthquake devastated the town of Tabas with more than 80 percent loss of its population, and severely damaged over 90 outlying villages with distances up to 80 km from Tabas city (Shoja-Taheri and Anderson 1988). The total death toll has been estimated to exceed 15,000 (Berberian 1979a; Mohajer-Ashjai and Nowroozi 1979).

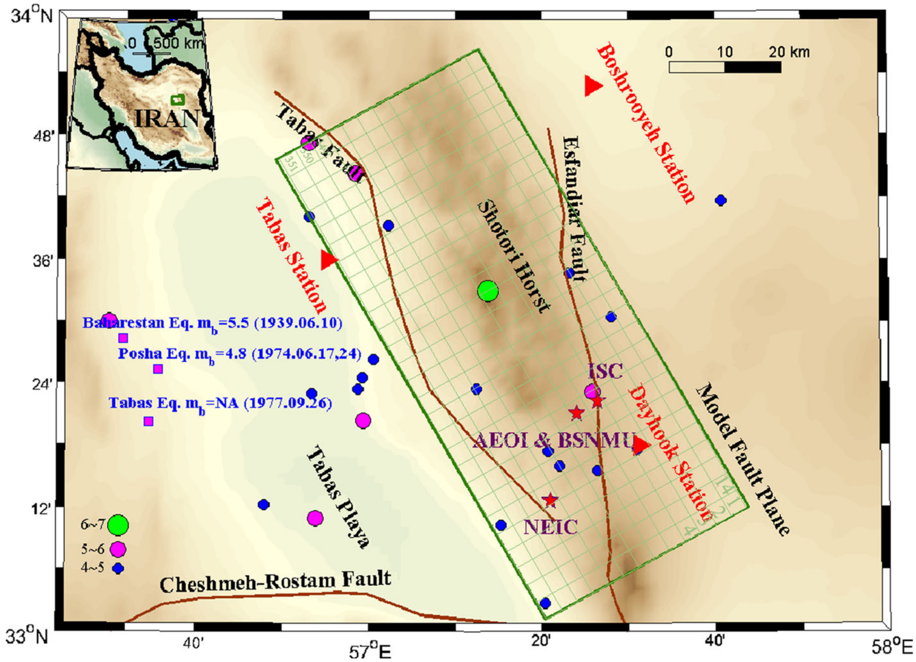

Fig. 1 Geographical scope of the simulation. The *color* scheme reflects topography, with the *color green* denoting low elevation and the *color brown* denoting mountains. The *red triangles* represent the three near-fault stations at which the simulations are realized. The surface projection of the Tabas model is also shown, as well as the approximate location of the fault traces. The fault plane is divided into 351 sub-faults. The *magenta squares* demonstrate a few twentieth-century earthquakes which caused some local damage in the vicinity of Tabas before the earthquake of September 16, 1978, Tabas (Berberian 1979a, b) and the background seismicity of the region ($4 \leq M \leq 6.5$). The three *red asterisks* illustrate various estimates of the Tabas hypocentral locations, based on regional networks and teleseismic recordings

The Tabas earthquake is significant, not only because of its great destruction, but also because of the unique collection of strong-motion records produced by this earthquake. These strong-motion records represent one of the most complete set of accelerograms for a shallow, intraplate, thrust earthquake with magnitude greater than 7 (Hartzell and Mendoza 1991).

In addition, some of the ground-motion records (GMRs) from Tabas earthquake can be classified as near-field records. The near-fault effects can be considerably different from far-field effects. The first earthquake with a near-fault effect that was of interest to engineers and seismologists was the 1971 San Fernando California earthquake. The issue of near-field earthquakes gained more attention among scientists after the Northridge earthquake of 1994 (Beresnev and Atkinson 1998b) and Hyogo-Ken Nanbu earthquake of 1995 (Furumura and Koketsu 1998) since these earthquakes provided valuable information about structural performance of engineered structures in the near-fault zone.

As a reasonable deduction, earthquakes with characteristics akin to the Tabas earthquake are rare. However, for studying the structural behavior of buildings during the Tabas earthquake, we need a set of GMRs to perform linear/nonlinear dynamic analyses. Unfortunately, like many other regions in the world, Iran's central seismic zone faces the problem of lack of sufficient GMRs. To overcome this issue and make up the required number of GMRs, seismic building codes such as ASCE, 7-2005, allow implementing appropriate simulated GMRs.

The main objective of the present study is to provide appropriate simulated GMRs from the Tabas earthquake to make the way forward for retrofitting existing structures and development of empirical fragility functions.

According to Hartzell and Mendoza (1991), "eleven SMA-1 strong-motion instruments were triggered by the Tabas earthquake in the distance range of 3–350 km from the surface rupture, their peak accelerations ranging from nearly 0.01–0.95 g. Of these sites, three are close enough to have sufficient amplitude to make them usable in a waveform inversion study. These three stations are Tabas, Dayhook, and Boshrooyeh." Therefore, we simulated Tabas earthquake at the Tabas, Dayhook and Boshrooyeh stations using the hybrid approach. Their locations are indicated in Fig. 1.

For this purpose, the grid search method is applied to increase similarity between the three simulated components (L, T and V) of ground shaking and observed data. The computer software AXITRA and EXSIM12 are used for synthesizing seismograms at low and high frequencies, respectively. Zafarani et al. (2012, 2013) used this method to simulate ground-motions from possible earthquake scenarios in the greater Tehran region. In the simulation procedure, the accepted criterion of the goodness-of-fit of synthetic seismograms is Anderson's criteria (Anderson 2004).

2 Simulation method

2.1 Synthesizing seismograms at low and high frequencies

In order to simulate broadband ground-motion time histories in the near field, one should synthetize both low- and high-frequency components of ground motions. It is a common procedure to synthetize low frequencies (0.1–1.0 Hz) with the deterministic approach. Nonetheless, random features of high-frequency ranges (1.0–20.0 Hz) cannot be modeled within a deterministic framework. Hartzell et al. (1999) have emphasized the applicability of the hybrid approach as the most suitable method for calculating ground motions in the near field of a finite fault over a wide frequency range from 0.1 to 20 Hz. Therefore, we used a hybrid method to combine the deterministic simulation of the low frequencies with a stochastic simulation of the high frequencies to synthetize broadband ground-motion time histories. In this study, the transition frequency between high- and low-frequency portions is set at 1.0 Hz. Moreover, detailed information regarding simulation of low- and high-frequency components of ground motions is provided in the next few sections.

2.2 Low-frequency components (f < 1.0 Hz)

The three-dimensional (3-D) wave propagation may be considered to realistically model the process of rupture propagation. However, by assuming a 3-D model, we cannot accurately apply this approach for the Tabas region since sufficient information on the soil structure mechanical characteristics and the active dynamic fault systems in the study region is not available. Therefore, we assumed a one-dimensional (1-D) layer for the earth's crust. This assumption makes the problem of wave propagation much easier to be dealt with. In this study, a discrete wavenumber/finite-element method implemented in the AXITRA code (Bouchon 2003) is used to simulate ground motions at low frequencies. The discrete wavenumber method is one of the most useful methods to verify the accuracy of other methods like finite-difference, finite-element, and ray methods, mode summation or pseudo-spectral techniques.

2.3 High-frequency components (f > 1.0 Hz)

Many seismologists and engineers worldwide have already used the stochastic finite-fault method in their scientific endeavors. This method is a generalization and extension of the simple stochastic method of Boore (1983). The simple stochastic method has been widely used for simulating and predicting earthquake ground motions for engineering purposes. In the stochastic finite-fault method, a large fault can be divided into small sub-faults so as to consider each unit as a point source. Further information related to the basic idea behind this method could be found in Hartzell (1978) and Kanamori and Stewart (1978). Beresnev and Atkinson (1997) and Silva et al. (1990) used the stochastic finite-fault method, with the use of stochastic Green's functions for generating high-frequency components of ground motion. The stochastic finite-fault method was first implemented in the computer code FINSIM in 1998 (Beresnev and Atkinson 1998a), and since then, it has been modified several times and widely used in different regions (e.g. Chopra et al. 2012a, b; Yalcinkaya et al. 2012; Zafarani et al. 2009, 2015). The computer code EXSIM presented by Motazedian and Atkinson (2005) has significantly improved FINSIM by eliminating the conceptual deficiency of the FINSIM. EXSIM is a FORTRAN-based open-source program that generates time series of earthquake GMRs using the stochastic finite-source simulation algorithm. The newer version of EXSIM, i.e., STRESSSIM, was then developed by Assatourians and Atkinson (2007) to consider the effect of non-uniform stress distribution on the fault by combining the stochastic finite-fault method with an inversion algorithm. STRESSSIM has been successfully applied for deriving the stress-drop distribution of three California earthquakes (Assatourians and Atkinson 2010). EXSIM was eventually upgraded by Karen Assatourians and Gail Atkinson, in May 2012 to incorporate the improvements suggested by Boore (2009). The latest version of EXSIM is known as EXSIM12. EXSIM12 is a stochastic finite-fault algorithm to generate acceleration time histories for specified earthquake fault rupture scenarios, where the ruptures are specified by a few simple metrics such as earthquake magnitude and distance. This program provides users with options to include more detailed information on fault geometry and slip, or net propagation effects. In EXSIM12, by defining the hypocenter as well as rupture velocity on the fault, and supposing radial propagation from the hypocenter and appropriate triggering time for each sub-event, it is possible to construct the total motion at each point as the sum of the contribution from all sub-events.

2.4 Combination of low- and high-frequency components

In the time domain, low frequencies are combined with high frequencies, resulting in the broadband seismogram that spans the entire frequency range of interest (e.g., Mai and Beroza 2003). Using the scheme defined in Eq. 1, the time traces calculated by the two techniques are reconciled at intermediate frequencies where their domain of validity overlaps:

$$\mathrm{BB}(t) = F^{-1}[w_{\mathrm{l}}\mathrm{LF}(f)] + F^{-1}[w_{\mathrm{h}}\mathrm{HF}(f)] \quad (1)$$

where BB is the broadband spectrum and LF and HF are the low- and high-frequency spectra, respectively. F^{-1} indicates the inverse Fourier transform; and w_{l} and w_{h} are two smoothed frequency-dependent weighting functions. The two signals are weighted in the transition band such that at each frequency the weighting functions add up to unity. Using 1 Hz as a transition between high- and low-frequency components is well established, see, e.g., (Bielak et al. 2010; Ameri et al. 2012; Olsen et al. 2006). This is generally attributable to the maximum resolved frequency of coherent motions around this value. This constraint is to a large extent due to the low resolution of velocity and crustal models. The complexity and inconsistency of high-frequency wavefields generated by the rupture propagation process also has an effect on the fault plane.

3 Source geometry of the Tabas fault

3.1 Hypocenter

The Tabas active fault was a thrust at the base of a series of low foothills made up to Neogene clay deposits which separate the Shotori fold-thrust mountain belt (in the east) from the Tabas compressional depression (in the west) (Fig. 1) (Berberian 1982)

Various estimates of the Tabas hypocentral locations, based on regional networks [e.g., Atomic Energy Organization of Iran (AEOI) and Bulletin of the Seismographic Network of Mashhad University (BSNMU)] and teleseismic recordings [e.g., National Earthquake Information Center (NEIC) and International Seismological Centre (ISC)], are available (Berberian 1982; Engdahl et al. 1998; Hartzell and Mendoza 1991) (see Fig. 1).

3.2 Strike, dip and rake and fault dimensions

To this date, various strike, dip and rake values have been reported for the Tabas earthquake using several methods listed in Table 1. All the studies except Walker et al. (2003) propose relatively the same values for the mentioned parameters. The result given by Hartzell and Mendoza (1991) based on forward modeling of WWSSN P waves was used in this study, and accordingly, the strike, dip and initial rake angle are assumed to have values of 330°, 25° and 110°, respectively.

The length and width of the Tabas fault plane were estimated as 85 and 25 km respectively, based on the empirical relationship developed by Wells and Coppersmith (1994). These values are consistent with the findings of Berberian (1979a) and Berberian et al. (1979) (length = 85 km; width = 23 km) and Walker et al. (2003) (length = 90 km). Here, following Hartzell and Mendoza (1991), the fault length and fault width are assumed equal to 95 and 45 km in turn. Hartzell and Mendoza (1991) have selected these values for dimensions of the Tabas fault based on three main factors, namely observed ruptured area, geometrical spreading of aftershocks and forward modeling of WWSSN P waves.

4 Simulation parameters

Fourier spectral amplitudes of high-frequency components of strong earthquake ground acceleration are a function of source, path and site effects which can be expressed as follows:

Table 1 Source parameters reported for the September 16, 1978, Tabas mainshock

Origin times	Epicenter	Focal depth (km)	M_w or M_s	Length and width of the fault (km)	Strike (°)	Dip (°)	Rake (°)	Method	References
15:36:56	33.145°N 57.340°E	42	$M_s = 7.7$	65 × 37	332	31	107	Inversion of long-period P-wave first motion data	Berberian et al. (1979)
15:35:56	33.386°N 57.434°E	33	$M_w = 7.4$	–	330	30	110	Inversion of long-period surface waves	Niazi and Kanamori (1981)
15:36:13	33.386°N 57.434°E	11	$M_w = 7.3$	–	328	33	107	CMT solution	Global CMT Catalog
15:35:56	33.218°N 57.322°E	20	$M_s = 7.4$ $m_b = 6.5$	95 × 45	330	25	110	Forward modeling of WWSSN P-waves	Hartzell and Mendoza (1991)
–	33.25°N 57.38°E	–	$M_w = 7.3$	65 × 17	355	16	155	Inversion of P- and SH-waveforms	Walker et al. (2003)
15:35:56	–	–	$M_w = 7.4$	95 × 45	330	25	125	Grid search	This paper

$$Y(M_0, R, f) = E(M_0, f) \cdot P(R, f) \cdot G(f) \cdot I(f) \tag{2}$$

where $Y(M_0, r, f)$ is the total spectrum of the motion at a site; $E(M_0, f)$, $P(R, f)$, $G(f)$ and $I(f)$ are source, path, site and type of motion, respectively, and M_0 is the seismic moment (Boore 2003). Important parameters for simulation of high- and low-frequency components are described below.

4.1 Site and path effects

Path effect in Boore (2003) is expressed as follows:

$$P(R,f) = Z(R)\exp\left(\frac{-\pi f R}{Q(f)\, c_Q}\right) \tag{3}$$

$Z(R)$ is a geometrical spreading function used for path effect attenuation. This factor is adopted from Hassani et al. (2011) who have proposed the following equation to describe geometrical spreading based on the average depth of the Moho in the east-central region of Iran:

$$Z(R) = \begin{cases} R^{-1} & \text{for } R < 60 \text{ km} \\ (R.60)^{-0.5} & \text{for } R \geq 60 \text{ km} \end{cases} \quad (R \text{ is the hypocentral distance}) \tag{4}$$

$Q(f) = 151f^{0.75}$ is a S-wave attenuation which is also adopted from Hassani et al. (2011). In order to obtain the Q function, Hassani et al. (2011) utilized the generalized inversions of S-wave amplitude spectra and verified the results with similar studies. Meanwhile, c_Q is the seismic velocity used in the determination of $Q(f)$.

Site effect has been calculated based on the H/V method [see Motazedian (2006) for details]. Figure 2 shows the calculated values for east-central Iran in comparison with the

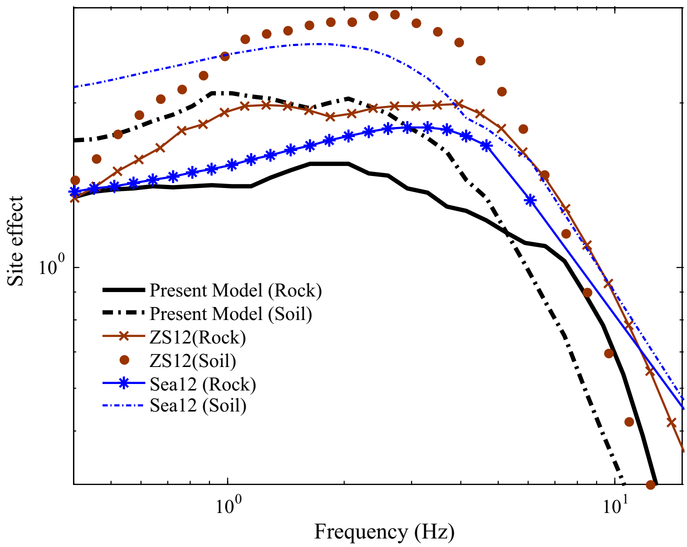

Fig. 2 Results of the present study for the site effect of central Iran in comparison with the results of other models. Zafarani and Soghrat (2012), ZS12; Soghrat et al. (2012), Sea12

previous studies for Zagros and northern Iran (Zafarani and Soghrat 2012; Soghrat et al. 2012).

4.2 Velocity and density model

One of the parameters for low-frequency component simulation is a 1-D crustal velocity model. This model is adopted from Berberian (1982). Berberian (1982) has selected velocity structure based on existing geologic data and a process of minimizing aftershock location residual errors. The P-wave and S-wave velocity profiles according to Berberian (1982) are listed in Table 2.

After determination of the velocity profile, we defined the density model based on the empirical rule proposed by Brocher (2005) as follows:

$$\rho = 1.6612\,V_{\mathrm{P}} - 0.4721\,V_{\mathrm{P}}^{2} + 0.0671\,V_{\mathrm{P}}^{3} - 0.0043\,V_{\mathrm{P}}^{4} + 0.000106\,V_{\mathrm{P}}^{5} \quad (5)$$

In Eq. 4, ρ is density in g/cm^3 and V_{P} is the P-wave velocity in km/s. Then, the P-wave velocity can be substituted into Eq. 4 to calculate the density and construct a 1-D layered model. In this research, slip distribution (Fig. 3) and stress drop, the other two important parameters are optimized by grid search methods.

4.3 Source parameters

Source effect based on Boore (2003) can be expressed as follows:

$$E(M_0, f) = C \cdot S(M_0, f) \cdot D(f, f_{\max}) \quad (6)$$

where C is a constant, S is the displacement source spectrum and $D(f, f_{\max}) = [1 + (f/f_{\max})^{2S}]^{-1/2}$ is the rapid decay of acceleration spectral levels beyond a frequency $f_{\max}$, while a number of researchers presented this parameter in another form. In the current research, we considered the relation proposed by Anderson and Hough (1984):

$$D(f, k) = \exp(-\pi f \kappa_0) \quad (7)$$

where κ_0 is the diminution parameter or zero-distance kappa factor. Already, generalized inversion of the S-wave amplitude spectra from the strong-motion data in the East-Central Iran has been used (Hassani et al. 2011) to estimate simultaneously source parameters, site response and the S-wave attenuation factor. They estimated a stress drop of 45 bars for the Tabas earthquake. According to previous studies performed in the Iranian plateau, kappa for horizontal and vertical components is considered to be equal to 0.05 and 0.02 in turn (Hassani et al. 2011).

Table 2 S- and P-wave velocity in addition to estimated densities for different values of depth

Depth (km)	$v_{\mathrm{P}}^{\mathrm{a}}$ (km/s)	$v_{\mathrm{S}}^{\mathrm{a}}$ (km/s)	Density[b] (g/cm^3)
0	3	1.7	2.23
2	5.3	2.8	2.59
24	6	3.6	2.72
43	6.8	3.9	2.92
44	8	4.7	3.30
50	8	4.8	3.30

[a] Based on Berberian (1982)

[b] Based on Brocher (2005)

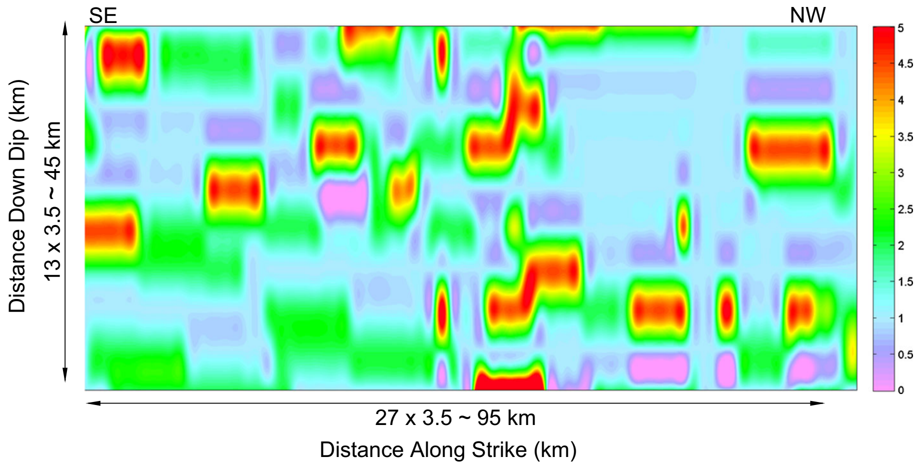

Fig. 3 Spatial distribution of the slip on the Tabas fault (slip distribution contoured in meters)

4.4 Sub-faults

In this paper, the fault plane is divided up into 351 sub-faults. These dimensions are a result of fitting 27 sub-faults along the strike of the fault and 13 sub-faults down the dip. Figure 1 illustrates that sub-faults have squared shapes with sides of about 3.5 km.

4.5 Rise time

To estimate rise time from empirical relations, we need to know the value of the seismic moment. Hartzell and Mendoza (1991) have determined the seismic moment for five slip models that are all based on triangular and Kostrov source time functions [see Table 1 in Saikia (1994) for more details]. In this paper, we calculated seismic moment from the Box car source time function since this function presents better results than other functions.

The seismic moment (M_0) is needed to calculate the amount of Rise time (T_r) (Hanks and Kanamori 1979):

$$\log M_0 = 1.5M_w + 16.1 \xrightarrow{Mw=7.4} M_0 = 1.58 \times 10^{27} \tag{8}$$

Between T_r and M_0, there are two empirical relationships (Silva et al. 1997; Somerville et al. 1999):

$$T_r = 2.03 \times 10^{-9} \times M_0^{1/3} \xrightarrow{M_0=1.58\times10^{27}} T_r = 2.37 \text{ s} \tag{9}$$

$$\log(T_r) = 0.33 \log(M_0) - 8.54 \xrightarrow{M_0=1.58\times10^{27}} T_r = 2.73 \text{ s} \tag{10}$$

As the above equations are empirical, several rise times have been imported in the simulation and results were compared with recorded strong-motion data of the Tabas earthquake. The resulted T_r from simulation ($T_r = 3.2$ s) which has a better compliance with recorded strong motion was selected (Table 3).

Finally, important modeling parameters are summarized and listed in Table 4.

Table 3 Average of Anderson criteria for several rise times that have been imported in the simulation

T_r (s)	Average of Anderson's criteria						Average
	Tabas FN	Tabas FP	Boshrooyeh FN	Boshrooyeh FP	Dayhook FN	Dayhook FP	
1	2.8	1.6	1.9	1.4	2.6	1.9	2.0
2	4.9	2.8	5.7	4.7	6.9	5.1	5.0
3	6.2	5.9	6.3	5.4	7.6	7.3	6.4
4	7.0	7.5	5.6	5.4	6.9	7.2	6.6
3.5	6.8	6.7	5.2	5.6	7.2	7.5	6.5
3.2	7.9	8.2	7.3	6.3	8.2	7.1	7.5

FN fault normal, *FP* fault parallel

Table 4 Input modelling parameters for the Tabas earthquake simulation

Parameters/items	Values and references
Length of fault	95 km (Hartzell and Mendoza 1991)
Width of fault	45 km (Hartzell and Mendoza 1991)
M_w	7.4 (Sarkar et al. 2005)
Fault orientation (strike, dip, rake angle)	330°, 25°, 125° (Hartzell and Mendoza 1991 and this study)
Near-surface attenuation: κ_h , κ_v	0.05, 0.02 s (Hassani et al. 2011)
Anelastic attenuation	$Q(f) = 151f^{0.75}$ (Hassani et al. 2011)
Site effects	$H/_V\ e^{-\pi k_v f}$ (this study)
T_r	3.2 s (this study)
Number of sub-faults	$27 \times 13 = 351$ (this study)
Slip distribution	Grid search method (this study) (see Fig. 3)
Stress drop	Grid search method (this study) ($\Delta\sigma = 150$ bar)
Stress_ref	70 bar
V_r	0.8 V_s
Source time function	Ramp function
Type of window	Saragoni–Hart

5 Strong-motion data and validation criteria

5.1 Correction of the recorded ground motions

The three components of the acceleration, velocity and displacement ground motion of the Tabas earthquake time histories recorded by the Tabas, Dayhook and Boshrooyeh stations are shown in Fig. 4. An interesting point about the Tabas station record is the location of the velocity pulse. The pulse in this time history occurs closer to the middle, while this pulse typically occurs at the beginning of the record. In addition, acceleration pulse in this record is not highlighted (Yaghmaei-Sabegh and Tsang 2011). The strong-motion data have been recorded on the Kinemetrics SMA-1 Analogue Strong-Motion Accelerographs

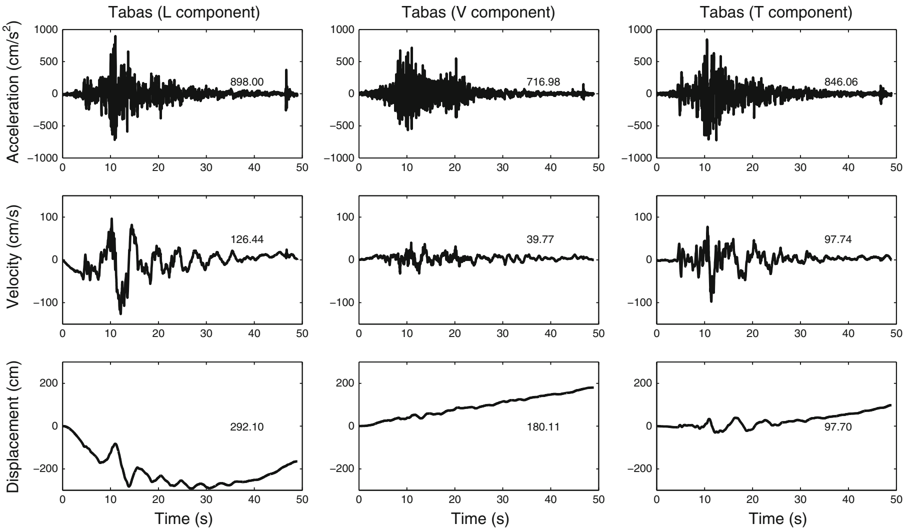

Fig. 4 Acceleration, velocity and displacement time histories of 1978 Tabas earthquake recorded at the Tabas station (*L*, *V*, *T* components)

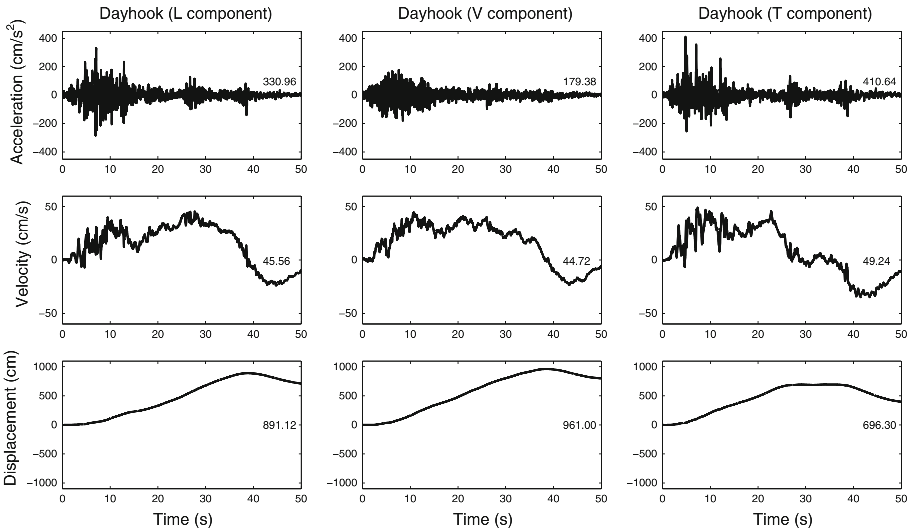

Fig. 5 Acceleration, velocity and displacement time histories of 1978 Tabas earthquake recorded at the Dayhook station (*L*, *V*, *T* components)

of the Iranian Strong-Motion Network (ISMN) of the Building and Housing Research Center (BHRC).

As shown in Figs. 4, 5 and 6, similar to the 24 major earthquakes of Iran examined by Zafarani et al. (2008), ground shakings of the Tabas earthquake are contaminated by ambient or instrumental noise. All acceleration time histories of the 24 major earthquakes of Iran with $M_w > 7.0$ were obtained by analog instruments of the Road, Housing & Urban

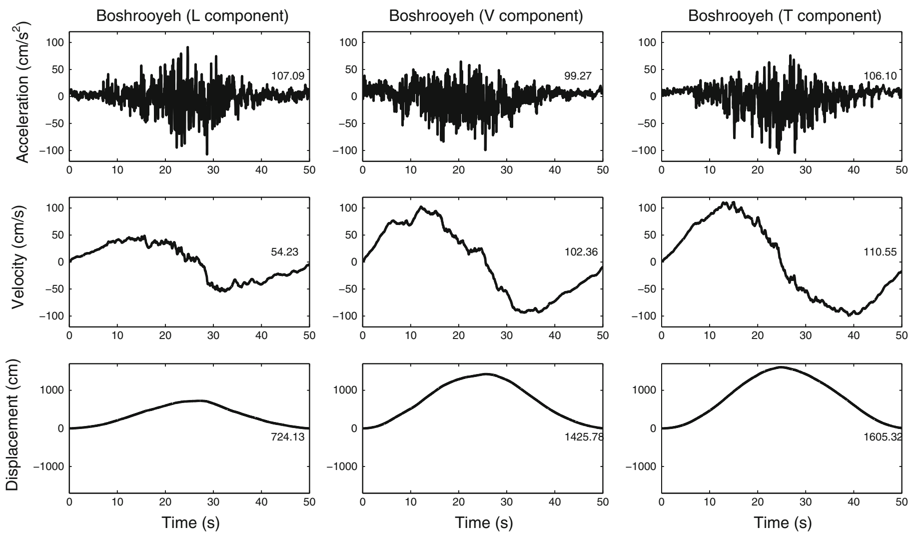

Fig. 6 Acceleration, velocity and displacement time histories of 1978 Tabas earthquake recorded at the Boshrooyeh station (*L*, *V*, *T* components)

Development Research Center of Iran (BHRC). Using the conventional filtering method, only three out of 27 records of Tabas (Hartzell and Mendoza 1991) and 15 out of 68 records of Manjil (1990, $M_w = 7.1$) (Niazi and Bozorgnia 1992) earthquakes have been corrected and other important records of these events remained useless, due to the mathematical limitations of the method (Ansari et al. 2010). To fix this problem, the useful nonlinear and adaptive de-noising method (i.e., wavelet de-noising method) have been used here.

In this paper, we used the modified wavelet de-noising method proposed by Ansari et al. (2007) to remove non-stationary and high-energy noise from time histories of the Tabas earthquake. The modified wavelet de-noising method is a two-step method that initially applies the correction to acceleration time histories and then removes the noise of moderate- and low-frequency components by applying the correction to velocity time histories. Figures 7, 8 and 9 show corrected time histories recorded at the Tabas, Dayhook and Boshrooyeh stations.

In addition, for a comparison between recorded and simulated time histories of Tabas earthquake, the recorded time histories were rotated by a simple vector rotation method, as introduced by Somerville et al. (1997), to the fault-normal and fault-parallel directions, as shown in Figs. 7, 8 and 9.

5.2 Validation criteria

The results of simulation were validated by comparing the simulated shape of the normalized integrals of acceleration (C1) and velocity (C2) squared, the Arias intensity (C3), the integral of velocity squared (C4), the peak acceleration (C5), peak velocity (C6), peak displacement (C7), acceleration response spectrum (C8) on a frequency-by-frequency basis, the Fourier spectrum (C9) and the cross-correlation (C10) with the observed time-series data (Anderson 2004).

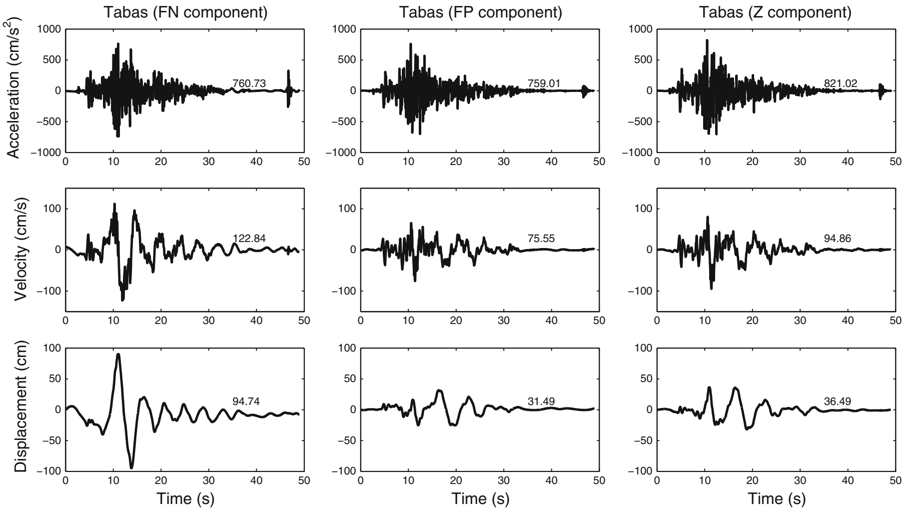

Fig. 7 Acceleration, velocity and displacement time histories of the 1978 Tabas earthquake corrected by the modified wavelet de-noising method proposed by Ansari et al. and rotated using a simple vector rotation method, as introduced by Somerville et al. (1997) at the Tabas station (fault-normal, fault-parallel and Z-direction components) (large velocity pulses in the fault-normal component of Tabas station are clearly obvious)

Anderson (2004) has compared each characteristic on a scale from 0 to 10, where a score of 10 means a perfect agreement. He has averaged scores for each parameter to yield an overall quality of fit. Scores in ranges of 0–4, 4–6, 6–8 and 8–10 represent poor, fair, good and excellent fit, respectively.

As mentione above, here slip distribution (Fig. 3) and stress drop, the other two important parameters are optimized by grid search methods.

6 Results

6.1 Simulated ground motions in the Tabas earthquake

In this study, a hybrid method is used to combine the deterministic simulation of the low frequencies with a stochastic simulation of the high frequencies for synthetizing broadband ground-motion time histories.

In Table 5, near-field accelerograph station data of the Tabas earthquake are represented (Shoja-Taheri and Anderson 1988). Also, the location of these stations is illustrated in Fig. 1.

The performance of the hybrid method is demonstrated in Figs. 10, 11 and 12, where it is compared the broadband simulated and recorded acceleration and velocity time histories in the Tabas, Dayhook and Boshrooyeh stations, respectively. Meanwhile, the right part of these figures demonstrated the Anderson's coefficient (CMEAN). CMEAN is the mean of C1–C9. C10 was dismissed because of the most difficult of all of the parameters to achieve a high score (Anderson 2004). The results of the Anderson's coefficient in the Tabas, Dayhook and Boshrooyeh stations indicated an excellent and good fit. In most cases, the

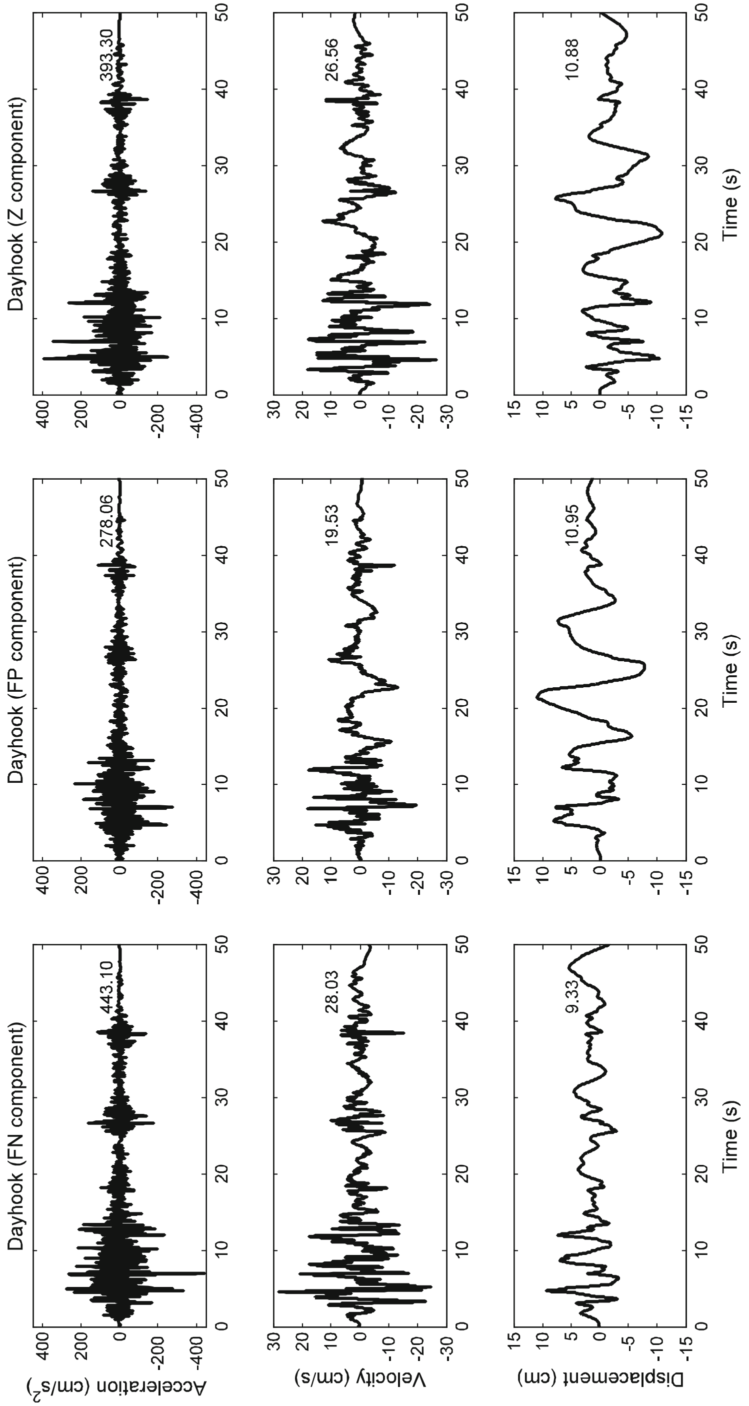

Dayhook (FN component)
Dayhook (FP component)
Dayhook (Z component)
Acceleration (cm/s^2)
Velocity (cm/s)
Displacement (cm)
Time (s)
443.10
278.06
393.30
28.03
19.53
26.56
9.33
10.95
10.88

◀**Fig. 8** Acceleration, velocity and displacement time histories of the 1978 Tabas earthquake corrected by the modified wavelet de-noising method proposed by Ansari et al. and rotated using the simple vector rotation method, as introduced by Somerville et al. (1997) at the Dayhook station (fault-normal, fault-parallel and Z-direction components)

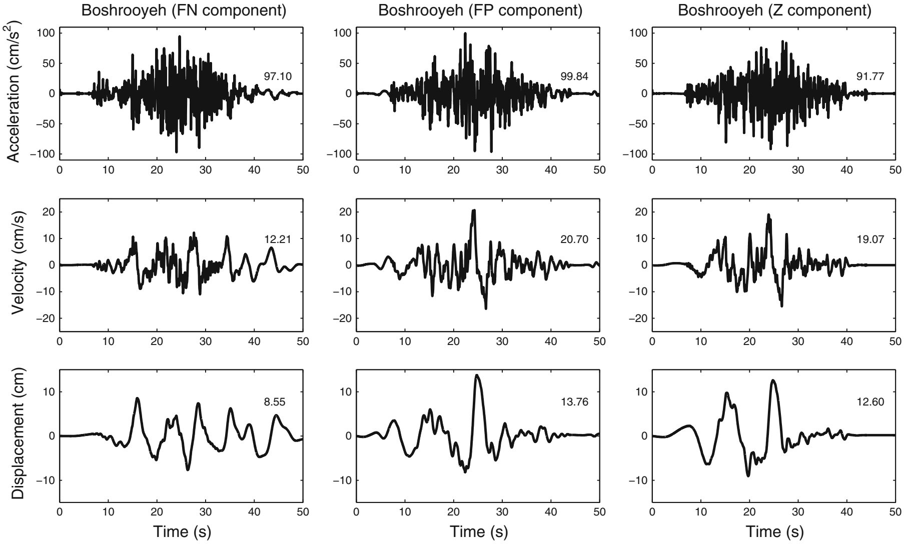

Fig. 9 Acceleration, velocity and displacement time histories of the 1978 Tabas earthquake corrected by the modified wavelet de-noising method proposed by Ansari et al. and rotated using simple vector rotation method, as introduced by Somerville et al. (1997) at the Boshrooyeh station (fault-normal, fault-parallel and Z-direction components)

Table 5 Near-field accelerograph station data from the Tabas earthquake (Shoja-Taheri and Anderson 1988)

No.	Station name	Latitude (°N) Longitude (°E)	Component orientation	*PGA* (cm/s^2)	*PGV* (cm/s)
1	Tabas	33.60	N74E (L)	867.0	100.0
		56.92	UP (V)	732.0	37.5
			N16W (T)	911.0	111.6
2	Dayhook	33.30	N80W (L)	366.0	20.6
		57.52	UP (V)	185.0	11.7
			S10W (T)	393.0	24.7
3	Boshrooyeh	33.88	N79E (L)	104.0	13.4
		57.43	UP (V)	76.0	13.8
			N11W (T)	84.0	15.6

peak values of acceleration, velocity and displacement are well matched. The average Anderson's coefficient for each site is listed in Table 6.

The corresponding 5% damped response spectra are also compared. The three components of near-field ground shaking recorded and simulated at the Tabas, Dayhook and

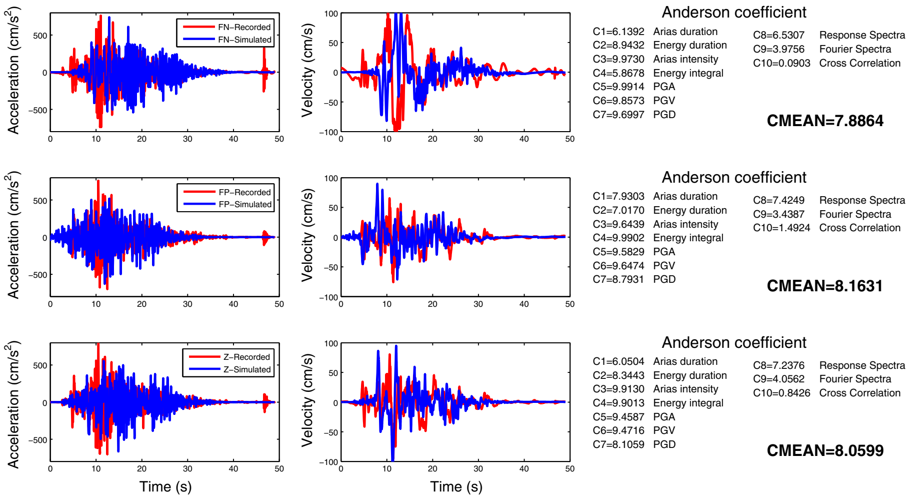

Fig. 10 Illustration of the broadband simulated acceleration and velocity time histories with those of the observed data and Anderson's coefficient at the Tabas station (fault-normal, fault-parallel and Z-direction components)

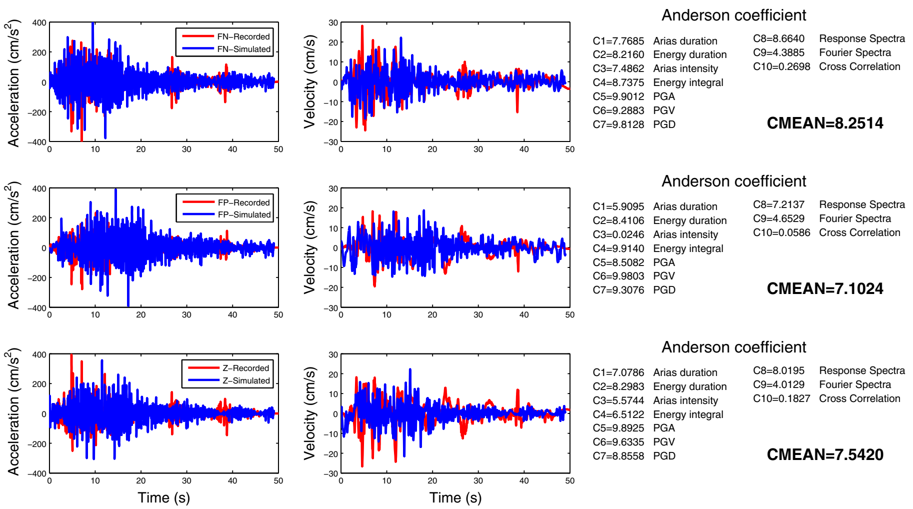

Fig. 11 Illustration of the broadband simulated acceleration and velocity time histories with those of the observed data and Anderson's coefficient at the Dayhook station (fault-normal, fault-parallel and Z-direction components)

Boshrooyeh stations are plotted in Figs. 13, 14 and 15. In Fig. 13, pseudo-acceleration response spectra are plotted. It is shown that the simulation results are broadly compatible with the observed time histories. Also, pseudo-velocity and displacement response spectra are illustrated in Figs. 14 and 15.

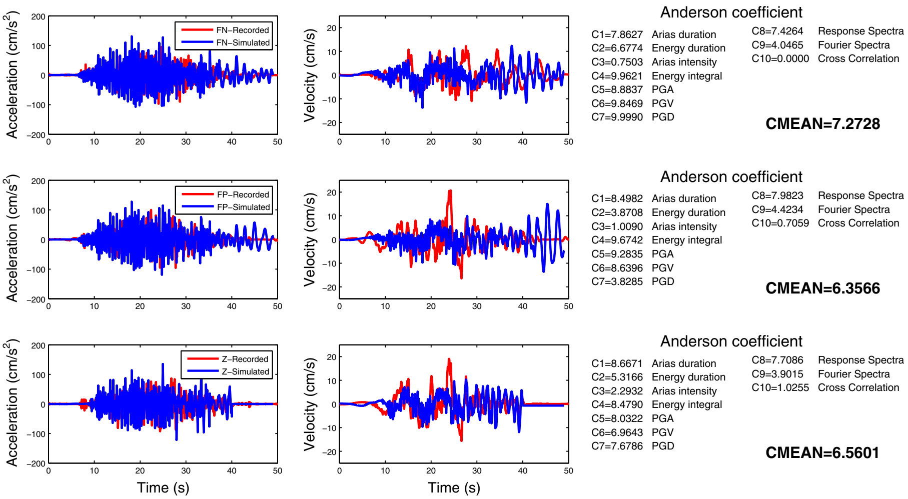

Fig. 12 Illustration of the broadband simulated acceleration and velocity time histories with those of the observed data and Anderson's coefficient at the Boshrooyeh station (fault-normal, fault-parallel and Z-direction components)

Table 6 Anderson's coefficient of the three stations of the Tabas earthquake time histories for our model and the Hartzell and Mendoza (1991) model

No.	Station name	Components	Anderson's coefficient	Quality of fit	Average of Anderson's coefficient	Overall quality of fit
1	Tabas	Fault normal	7.89	Good	8.04 & 6.67[a]	Excellent
		Fault parallel	8.16	Excellent		
		Z-direction	8.06	Excellent		
2	Dayhook	Fault normal	8.25	Excellent	7.63 & 6.1.6[a]	Good
		Fault parallel	7.10	Good		
		Z-direction	7.54	Good		
3	Boshrooyeh	Fault normal	7.27	Excellent	6.73 & 2.63[a]	Good
		Fault parallel	6.36	Good		
		Z-direction	6.56	Good		

[a] Average of Anderson's coefficient for the Hartzell and Mendoza (1991) model

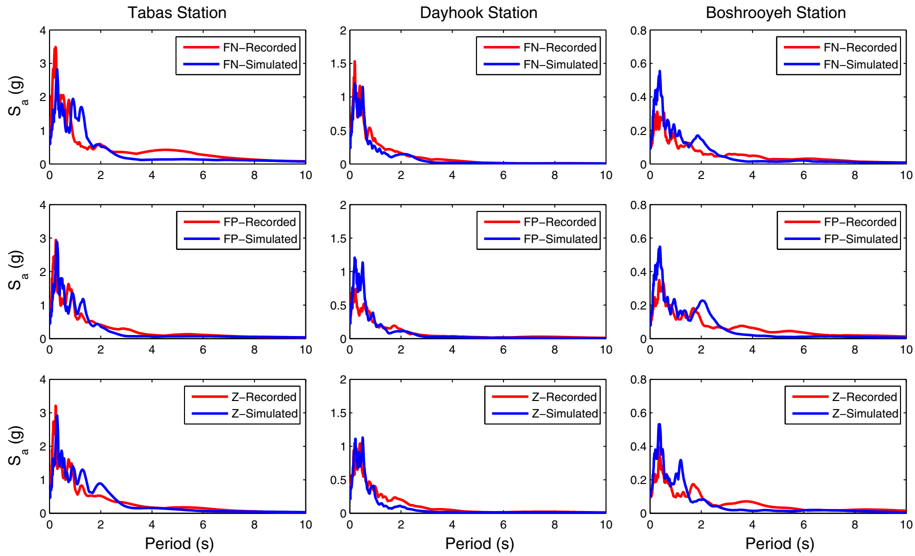

Fig. 13 Illustration of the broadband recorded and simulated pseudo-acceleration response spectra (5% damped) based on a hybrid low-frequency/high-frequency approach for three components of the Tabas, Dayhook and Boshrooyeh stations (fault-normal, fault-parallel and Z-direction components)

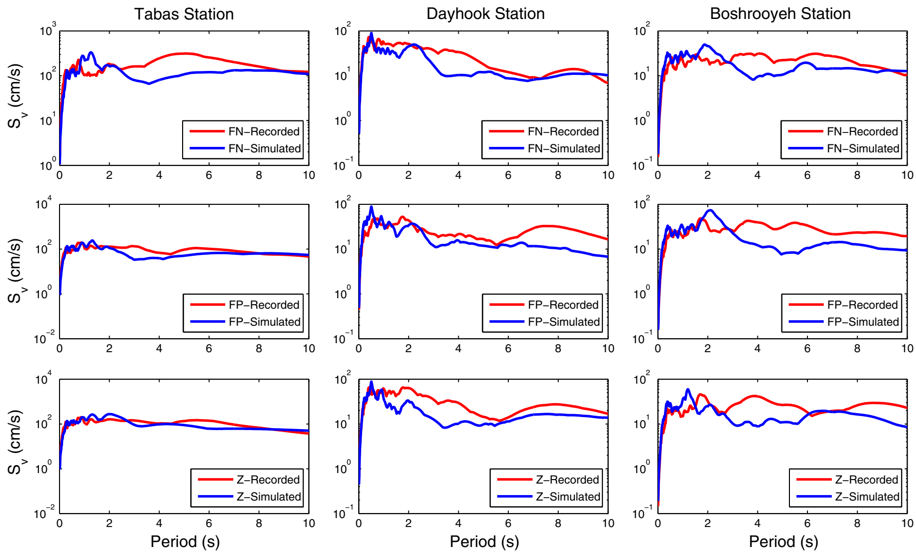

Fig. 14 Illustration of the broadband recorded and simulated pseudo-velocity response spectra (5% damped) based on a hybrid low-frequency/high-frequency approach for three components of the Tabas, Dayhook and Boshrooyeh stations (fault-normal, fault-parallel and Z-direction components)

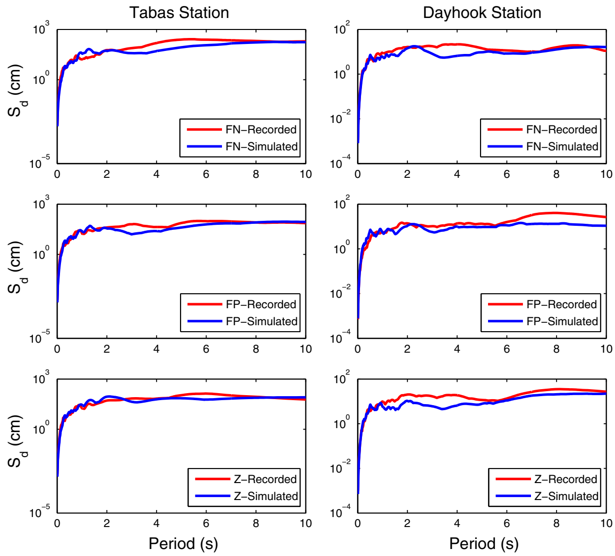

Fig. 15 Illustration of the broadband recorded and simulated displacement response spectra (5% damped) based on a hybrid low-frequency/high-frequency approach for three components of the Tabas, Dayhook and Boshrooyeh stations (fault-normal, fault-parallel and Z-direction components)

6.2 Validation by comparing the simulated ground motions with the Modified Mercalli Intensity (MMI)

After finding optimal parameters, especially slip distribution and stress drop, for the simulation of the Tabas earthquake and verification of these parameters, the simulated ground motions are compared with the Modified Mercalli Intensity observations.

By using parameters obtained from the hybrid method, simulation was performed for 17 towns and villages. To compare the simulated motions for these villages, the correlation equation of seismic intensity scales with the PGAs and PGVs (Eqs. 11, 12) proposed by Wald et al. (1999) is employed.

$$I_{\mathrm{mm}} = 3.66 \log(\mathrm{PGA}) - 1.66 \tag{11}$$

$$I_{\mathrm{mm}} = 3.47 \log(\mathrm{PGV}) + 2.35 \tag{12}$$

It should be considered that the equations proposed by Wald et al. (1999) have been used in different seismotectonic regions, e.g., India (Hough et al. 2002), that is, an intraplate region and China (Wang and Zhou 2006). There is some doubt regarding the application of these equations (Wald et al. 1999) to an intraplate region as was mentioned by Hough et al. (2002):

“One must also consider the possibility that a PGA–MMI relationship determined for earthquakes in California is not appropriate for an intraplate region. In particular, it has been suggested that, by virtue of having a higher average stress drop, intraplate ground motions might be characterized by a higher level of high-frequency energy and therefore be more damaging (to some types of structures especially) than those from comparable earthquakes in interplate regions.”

However, since both the California and Iranian plateaus have similar interplate regimes, the uncertainty is low. This is due to the fact that the PGA–MMI relationships have greater dependency on earthquake type than on construction type.

Berberian (1979b) reported the level of intensity on the Modified Mercalli Intensity Scale by presenting an intensity map (see figure 1 in Berberian 1979b) based on earth effects and observed effects on the towns and villages around the epicenter of Tabas earthquake. Table 7 illustrates the observed intensity of some stations near the epicenter based on the Berberian (1979b) report. The simulated seismic intensity associated with the simulated PGAs and PGVs for the 17 towns and villages around the epicenter of Tabas earthquake is also listed in Table 7. The comparison shows generally good agreement between simulated and observed intensity at most of the stations.

Table 7 Seismic intensity for 17 towns and villages around the epicenter of the Tabas earthquake, associated with the observed damages and simulated PGAs and PGVs according to Berberian (1979a, b) observation and hybrid simulation method, respectively

No.	Station name	Latitude (°N)	Longitude (°E)	I_{mm} (Eq. 11) (Wald et al. 1999)	I_{mm} (Eq. 12) (Wald et al. 1999)	Intensity in MMI (Berberian 1979b)
1	Nastanj	33.98	56.63	VII–	VIII–	VI–
2	Shirgesht	34.00	56.83	VI	VIII	VI–
3	Deh mohamad	34.00	56.98	VII	VII	VI–
4	Robat-e Dahaneh	33.95	56.80	VII	VIII	VI+
5	Boshrooyeh	33.87	57.43	VI	VI	VI–
6	Bisheh	33.81	56.54	VI+	VII+	VI+
7	Khaneh Rokni	33.65	56.66	VII	VII–	VII–
8	Tabas	33.60	56.93	IX–	IX–	IX–X
9	Robat-e Chah Gonbad	33.50	57.64	VI+	VI	VI–
10	Mardonshah	33.46	56.63	VII–	VII–	VII–
11	Dayhook	33.29	57.51	VII+	VII	VII–
12	Howz-e Surji	33.30	56.66	VII–	VI+	VII-
13	Chah-e Ali Asghar	33.16	56.56	V+	VI	VI+
14	H.Haji	33.08	57.23	VIII+	VII+	VII+
15	Dehno Fakhrabad	33.01	57.68	VI+	VI	VI–
16	Righabad	33.02	56.99	VII–	VII–	VII–
17	Chesmeh Rostam	33.02	56.93	VII–	VI+	VII–

7 Summary and conclusion

This paper was allocated to simulating three components of near-field ground shaking recorded during the main shock at Tabas, Dayhook and Boshrooyeh stations of the September 16, 1978, Tabas ($M_w = 7.4$), Iran, earthquake, close to the causative fault. The Tabas earthquake is significant, not only because of the great destruction it caused, but also because of the unique collection of strong-motion records it produced. A 1-D crustal velocity model for the region has been employed, and broadband strong motions for such scenarios from a hybrid method composed of the discrete wavenumber method developed by Bouchon (Bouchon 1981; Cotton and Coutant 1997) and a stochastic modeling technique proposed by Beresnev and Atkinson (1997, 1998a, b) for finite faults, modified by Assatourians and Atkinson (2007) are used for generating seismograms at low (0.1–1.0 Hz) and high frequencies (1.0–20.0 Hz), respectively. Computations are linear and performed at bedrock level, thereby not taking any effect of local geological conditions into account. An additional uncertainty that has not been considered is potential basin effects. The results of the simulations performed in the present study indicate that the estimated rise time of 3.2 s and rupture velocity of 0.8 V_s are more reasonable values.

To calculate the slip distribution and stress drop, a grid search method is employed as a tool for inversion solution of the problem aimed at minimizing the differences between the recorded and simulated data in terms of the Anderson's (2004) goodness-of-fit criteria. The broadband simulated and recorded acceleration and velocity time histories have been compared in three stations. The average Anderson coefficient for Tabas, Dayhook and Boshrooyeh is 8.04, 7.63 and 6.73, respectively. The results of the Anderson's coefficient in the Tabas station indicate an excellent fit while in the Dayhook and Boshrooyeh stations they represent a good fit.

For removing the noise from the three stations of the Tabas earthquake time histories, a modified two-step method proposed by Ansari et al. (2007) has been used. In addition, for comparison between recorded and simulated time histories of Tabas, the recorded time histories were rotated by a simple vector rotation method, as introduced by Somerville et al. (1997), to the fault-normal and fault-parallel directions, as shown in Figs. 7, 8 and 9.

Figures 13, 14 and 15 illustrate the recorded and simulated pseudo-acceleration, pseudo-velocity and displacement response spectra (5% damped) of the parallel, normal and Z-direction component of motions recorded at the Tabas, Dayhook and Boshrooyeh stations that could accurately model near-field ground motion at both high- and low-frequency ranges.

Finally, by using parameters obtained from the hybrid method, the simulation was performed for 17 towns and villages around the epicenter of the Tabas earthquake. The comparison between observed intensity of some stations near the epicenter based on the Berberian (1979b) report and the simulated seismic intensity associated with the simulated PGAs and PGVs for the 17 towns and villages around the epicenter of Tabas earthquake shows generally good agreement at most of the stations.

Acknowledgements The generosity of Karen Assatourians and Gail Atkinson for providing us with the source code of the EXSIM12 program is gratefully acknowledged. Our sincere thanks go to Olivier Coutant for providing us with the AXITRA package to calculate near-source seismograms with the discrete wavenumber method. The authors acknowledge the Building and Housing Research Centre of Iran for providing them with the accelerograms and shear-wave velocities used in the current study. H. Zafarani thanks the continuing support of the International Institute of Earthquake Engineering and Seismology in the framework of the Probabilities of Earthquake Ruptures in Iran (PERSIA) project.

References

Ameri G, Gallovič F, Pacor F (2012) Complexity of the Mw 6.3 2009 L'Aquila (central Italy) earthquake: 2. Broadband strong motion modeling. J Geophys Res Solid Earth 117:B04308. doi:10.1029/2011JB008729

Anderson JG (2004) Quantitative measure of the goodness-of-fit of synthetic seismograms. In: 13th world conference on earthquake engineering conference proceedings, Vancouver, Canada, Paper

Anderson JG, Hough SE (1984) A model for the shape of the Fourier amplitude spectrum of acceleration at high frequencies. Bull Seismol Soc Am 74:1969–1993

Ansari A, Noorzad A, Zare M (2007) Application of wavelet multi-resolution analysis for correction of seismic acceleration records. J Geophys Eng 4:362

Ansari A, Noorzad A, Zafarani H, Vahidifard H (2010) Correction of highly noisy strong motion records using a modified wavelet de-noising method. Soil Dyn Earthq Eng 30:1168–1181

Assatourians K, Atkinson GM (2007) Modeling variable-stress distribution with the stochastic finite-fault technique. Bull Seismol Soc Am 97:1935–1949

Assatourians K, Atkinson GM (2010) Coseismic stress parameter of three California Earthquakes derived from the stochastic finite fault technique. J Seismolog 14:431–443

Berberian M (1976) An explanatory note on the first seismotectonic map of Iran; a seismotectonic review of the country. Geol Surv Iran 39:7–142

Berberian M (1979a) Earthquake faulting and bedding thrust associated with the Tabas-e-Golshan (Iran) earthquake of September 16, 1978. Bull Seismol Soc Am 69:1861–1887

Berberian M (1979b) Tabas-e-Golshan (Iran) catastrophic earthquake of 16 September 1978: a preliminary field report. Disasters 2:207–219

Berberian M (1982) Aftershock tectonics of the 1978 Tabas-e-Golshan (Iran) earthquake sequence: a documented active 'thin-and thick-skinned tectonic'case. Geophys J Int 68:499–530

Berberian M, Asudeh I, Bilham R, Scholz C, Soufleris C (1979) Mechanism of the main shock and the aftershock study of the Tabas-e-Golshan (Iran) earthquake of September 16, 1978: a preliminary report. Bull Seismol Soc Am 69:1851–1859

Beresnev IA, Atkinson GM (1997) Modeling finite-fault radiation from the ωn spectrum. Bull Seismol Soc Am 87:67–84

Beresnev IA, Atkinson GM (1998a) FINSIM–a FORTRAN program for simulating stochastic acceleration time histories from finite faults. Seismol Res Lett 69:27–32

Beresnev IA, Atkinson GM (1998b) Stochastic finite-fault modeling of ground motions from the 1994 Northridge, California, earthquake. I. Validation on rock sites. Bull Seismol Soc Am 88:1392–1401

Bielak J et al (2010) The ShakeOut earthquake scenario: verification of three simulation sets. Geophys J Int 180:375–404

Boore DM (1983) Stochastic simulation of high-frequency ground motions based on seismological models of the radiated spectra. Bull Seismol Soc Am 73:1865–1894

Boore DM (2003) Simulation of ground motion using the stochastic method. Pure appl Geophys 160:635–676

Boore DM (2009) Comparing stochastic point-source and finite-source ground-motion simulations: SMSIM and EXSIM. Bull Seismol Soc Am 99:3202–3216

Bouchon M (1981) A simple method to calculate Green's functions for elastic layered media. Bull Seismol Soc Am 71:959–971

Bouchon M (2003) A review of the discrete wavenumber method Pure and applied. Geophysics 160:445–465

Brocher TM (2005) Empirical relations between elastic wavespeeds and density in the Earth's crust. Bull Seismol Soc Am 95:2081–2092

Chopra S, Kumar D, Choudhury P, Yadav R (2012a) Stochastic finite fault modelling of M w 4.8 earthquake in Kachchh, Gujarat, India. J Seismolog 16:435–449

Chopra S, Kumar V, Suthar A, Kumar P (2012b) Modeling of strong ground motions for 1991 Uttarkashi, 1999 Chamoli earthquakes, and a hypothetical great earthquake in Garhwal-Kumaun Himalaya. Nat Hazards 64:1141–1159

Cotton F, Coutant O (1997) Dynamic stress variations due to shear faults in a plane-layered medium. Geophys J Int 128:676–688

Engdahl ER, van der Hilst R, Buland R (1998) Global teleseismic earthquake relocation with improved travel times and procedures for depth determination. Bull Seismol Soc Am 88:722–743

Furumura T, Koketsu K (1998) Specific distribution of ground motion during the 1995 Kobe earthquake and its generation mechanism. Geophys Res Lett 25:785–788

Hanks TC, Kanamori H (1979) A moment magnitude scale. J Geophys Res B 84:2348–2350

Hanks TC, McGuire RK (1981) The character of high-frequency strong ground motion. Bull Seismol Soc Am 71:2071–2095

Hartzell SH (1978) Earthquake aftershocks as Green's functions. Geophys Res Lett 5:1–4

Hartzell S, Mendoza C (1991) Application of an iterative least-squares waveform inversion of strong-motion and teleseismic records to the 1978 Tabas, Iran, earthquake. Bull Seismol Soc Am 81:305–331

Hartzell S, Harmsen S, Frankel A, Larsen S (1999) Calculation of broadband time histories of ground motion: comparison of methods and validation using strong-ground motion from the 1994 Northridge earthquake. Bull Seismol Soc Am 89:1484–1504

Hassani B, Zafarani H, Farjoodi J, Ansari A (2011) Estimation of site amplification, attenuation and source spectra of S-waves in the East-Central Iran. Soil Dyn Earthq Eng 31:1397–1413

Hough SE, Martin S, Bilham R, Atkinson GM (2002) The 26 January 2001 M 7.6 Bhuj, India, earthquake: observed and predicted ground motions. Bull Seismol Soc Am 92:2061–2079

Kanamori H, Stewart GS (1978) Seismological aspects of the Guatemala earthquake of February 4, 1976. J Geophys Res Solid Earth (1978–2012) 83:3427–3434

Khodaverdian A, Zafarani H, Rahimian M (2015) Long term fault slip rates, distributed deformation rates and forecast of seismicity in the Iranian Plateau. Tectonics 34:2190–2220

Mai PM, Beroza G (2003) A hybrid method for calculating near-source, broadband seismograms: application to strong motion prediction. Phys Earth Planet Int 137:183–199

Mohajer-Ashjai A, Nowroozi A (1979) The Tabas earthquake of September 16 1978 in east-central IranA preliminary field report. Geophys Res Lett 6:689–692

Motazedian D (2006) Region-specific key seismic parameters for earthquakes in Northern Iran. Bull Seismol Soc Am 96:1383–1395

Motazedian D, Atkinson GM (2005) Stochastic finite-fault modeling based on a dynamic corner frequency. Bull Seismol Soc Am 95:995–1010

Niazi M, Bozorgnia Y (1992) The 1990 Manjil, Iran, earthquake: geology and seismology overview, PGA attenuation, and observed damage. Bull Seismol Soc Am 82:774–799

Niazi M, Kanamori H (1981) Source parameters of 1978 Tabas and 1979 Qainat, Iran, earthquakes from long-period surface waves. Bull Seismol Soc Am 71:1201–1213

Olsen K, Akinci A, Rovelli A, Marra F, Malagnini L (2006) 3D ground-motion estimation in Rome, Italy. Bull Seismol Soc Am 96:133–146

Saikia CK (1994) Modeling of strong ground motions from the 16 September 1978 Tabas, Iran, earthquake. Bull Seismol Soc Am 84:31–46

Sarkar I, SriRam V, Hamzehloo H, Khattri K (2005) Subevent analysis for the Tabas earthquake of September 16, 1978, using near field accelerograms. Phys Earth Planet Inter 151:53–76

Shoja-Taheri J, Anderson JG (1988) The 1978 Tabas, Iran, earthquake: an interpretation of the strong motion records. Bull Seismol Soc Am 78:142–171

Silva W, Darragh R, Stark C, Wong I, Stepp J, Schneider J, Chiou S (1990) A methodology to estimate design response spectra in the near-source region of large earthquakes using the band-limited-white-noise ground motion model. In: Proceedings of Fourth US Conference on Earthquake Engineering, pp 487–494

Silva W, Abrahamson N, Toro G, Costantino C (1997) Description and validation of the stochastic ground motion model. Final Report Brookhaven National Laboratory

Soghrat M, Khaji N, Zafarani H (2012) Simulation of strong ground motion in northern Iran using the specific barrier model. Geophys J Int 188:645–679

Somerville PG, Smith NF, Graves RW, Abrahamson NA (1997) Modification of empirical strong ground motion attenuation relations to include the amplitude and duration effects of rupture directivity. Seismol Res Lett 68:199–222

Somerville P et al (1999) Characterizing crustal earthquake slip models for the prediction of strong ground motion. Seismol Res Lett 70:59–80

Wald DJ, Quitoriano V, Heaton TH, Kanamori H (1999) Relationships between peak ground acceleration, peak ground velocity, and modified Mercalli intensity in California. Earthq Spectra 15:557–564

Walker R, Jackson J, Baker C (2003) Surface expression of thrust faulting in eastern Iran: source parameters and surface deformation of the 1978 Tabas and 1968 Ferdows earthquake sequences. Geophys J Int 152:749–765

Wang G-Q, Zhou X-Y (2006) 3D finite-difference simulations of strong ground motions in the Yanhuai area, Beijing, China during the 1720 Shacheng earthquake (M s 7.0) using a stochastic finite-fault model. Soil Dyn Earthq Eng 26:960–982

Wells DL, Coppersmith KJ (1994) New empirical relationships among magnitude, rupture length, rupture width, rupture area, and surface displacement. Bull Seismol Soc Am 84:974–1002

Yaghmaei-Sabegh S, Tsang H (2011) An updated study on near-fault ground motions of the 1978 Tabas, Iran, earthquake (Mw = 7.4). Sci Iran 18:895–905

Yalcinkaya E, Pinar A, Uskuloglu O, Tekebas S, Firat B (2012) Selecting the most suitable rupture model for the stochastic simulation of the 1999 Izmit earthquake and prediction of peak ground motions. Soil Dyn Earthq Eng 42:1–16

Zafarani H, Soghrat M (2012) Simulation of ground motion in the Zagros region of Iran using the specific barrier model and the stochastic method. Bull Seismol Soc Am 102:2031–2045

Zafarani H, Mousavi M, Noorzad A, Ansari A (2008) Calibration of the specific barrier model to Iranian plateau earthquakes and development of physically based attenuation relationships for Iran. Soil Dyn Earthq Eng 28:550–576

Zafarani H, Noorzad A, Ansari A, Bargi K (2009) Stochastic modeling of Iranian earthquakes and estimation of ground motion for future earthquakes in Greater Tehran. Soil Dyn Earthq Eng 29:722–741

Zafarani H, Vahidifard H, Ansari A (2012) Sensitivity of ground-motion scenarios to earthquake source parameters in the Tehran metropolitan area, Iran. Soil Dyn Earthq Eng 43:342–354

Zafarani H, Vahidifard H, Ansari A (2013) Prediction of broadband ground-motion time histories: the case of Tehran, Iran. Earthq Spectra 29:633–660

Zafarani H, Rahimi M, Noorzad A, Hassani B, Khazaei B (2015) Stochastic simulation of strong-motion records from the 2012 Ahar–Varzaghan dual earthquakes, Northwest of Iran. Bull Seismol Soc Am 105:1419–1434